Technical Article

Physical and Numerical Investigations of Gas Turbine Blades Failure

H.R. Faridi[1], A. Momeni[1], M. Mohammadpour[1], V. Sarfarazi[2,*]

[1]Department of Materials Science and Engineering, Hamadan University of Technology, Hamadan, Iran.
[2]Department of Mining Engineering, Hamadan University of Technology, Hamadan, Iran.
Received: 15 July 2017 - Accepted: 27 August 2017

Abstract

Two blade samples from the first and second stages of a gas turbine were investigated to understand the reason of fracture. All samples suffered excessive heat superficially. Using a TBC layer on top of Diffusion coating will be a reasonable solution for protecting the blades. Although in case of the first stage blades cracking was postponed, the thermomechanical fatigue cracks still originated from the blade surface. It was observed that the damage of the thermal barrier coating layer would lead to the overheating of the blades, promoting the rate of creep and rafting of γ′ precipitates. This phenomenon was more severe in the second stage samples with more damaged protective layers. It was found that the chemical composition of the fuel gas may increase the potential and rate of corrosion and damage to the blades. Concurrent with physical investigation, numerical simulation was performed to study the effect of particle impact into the blade. By changing the particle radii and its position, damage area was inspected. Numerical simulation shows that particle radii and its position have an important effect on the chipping removal from the blade.

Keywords: Superalloys, γ′ Precipitates, Thermomechanical Fatigue, Mercaptans, Numerical Simulation.

1. Introduction

In today's technology, single and poly-crystal Ni-base super alloys are used vastly in gas turbines due to their excellent high temperature fatigue and creep properties. The modifications in alloy compositions, over years, has led to shift the properties such as; single crystal cast ability, γ to γ′ ratio, recrystallization propensity, carbide phase formation, alloy density, and hot corrosion properties. The coherent interface between the γ matrix and the γ′ particles withstand against the dislocations penetration and plays as the major strengthener in these alloys [1-3]. Creep and fatigue are critical damage mechanisms for turbine components because they operate within aggressive environments at high temperatures with excessive loadings. The mechanisms of creep and fatigue damages are strongly dependent on temperature and stress condition. It is thus important to analyze the type of damage to estimate the lifetime of components and to understand the limits. The as-cast turbine blades (typically made by investment casting) must undergo a series of heat treatments to achieve the desirable properties for use in engines. The major aims of heat treating are to reduce the compositional gradients and internal stresses throughout the material and subsequently dispersing a second phase within.
To obtain maximum strength in the alloy, aging treatment following homogenization allows the γ (to grow to the optimum size and become uniform) . The γ′ phase coarsening and the formation of topologically packed phases (TCP) can significantly deteriorate the microstructural stability of these alloys. The TCP phases, which are brittle intermetallic in nature, reduce the creep or fatigue resistance because they act as the stress concentrators within the material and remove the important strengtheners like Tungsten and Rhenium [4-8]. The high cycle fatigue induced failures in gas turbine blades often operates in combination with other damaging factors such as creep, low cycle fatigue, thermo-mechanical fatigue, hot corrosion, and oxidation. The fatigue cracks often form at the tip of the persistent slip bands (PSBs) especially where they interact with the casting pores and the carbides represent near the surface. Early crack propagations along the slip planes will be replaced later by non-crystallographic propagation of dominant cracks [9]. The gas turbine operation reliability in service is also dependent on the media composition as air, fuel gas, fuel oil, and water. Excess concentration of certain fuel components or contamination in one or more of the operation media could have detrimental effects on gas turbine components like valves, burners, blades, etc. The combustion behavior of the fuel to be used in a gas chamber dominates the turbine operation by its effect on corrosion and scaling properties of the components. The contents of condensable molecules in gaseous fuels such as hydrocarbons and water may cause corrosive salts. If the salts contain

*Corresponding author
Email address: sarfarazi@hut.ac.ir

chlorides, pitting corrosion underneath moist deposit is expected. Given the importance of this topic, there are a few systematic investigations considering the influence of chemical environment on the failure behavior of the blades [10-12]. This is due to the fact that the gas turbine accessories and components such as turbine blades either during operation or standstill times are susceptible to the oxidation and the hot corrosion. At temperatures over 980 °C, the oxidation of alloying elements such as Al and Cr becomes important and the hot corrosion is, more or less, triggered at the same temperatures by the presence of sulfur in fuel or salt in the environment [13,14]. Demanding operational conditions for gas turbine engines necessitates the use of a variety of thermal barrier coatings (TBC) [15,16]. Although TBC enhance the resistance of the alloy versus corrosion, they may also have side effects that lead to the premature failure of coated components via low-cycle and thermo-mechanical fatigue. These are often the limiting modes of degradation in gas turbines. Mismatch in the properties of the coating and the substrate alloy are responsible for aggravating the failure mechanism. The mismatch may arise due to differences in the thermal expansion coefficients, ductility, strength and elastic moduli, and significantly reduce the fatigue life. Therefore, it is very important to choose the best possible diffusion coating systems and an appropriate thermal barrier coating on top of it to prevent excessive thermal fatigue and low-cycle fatigue which will be very detrimental to the coating itself and consequently to the super-alloy hardware underneath of it [13]. The presented literature survey tried to cover different parameters which should be taken into account when speaking about the application of superalloys for high temperature applications, especially turbine blades. Although the individual influence of different structural and metallurgical parameters on the damage mechanisms of such components have been studied and documented, the mechanism of failure in practice, including all the mentioned parameters, has not been studied in detail. Hence, the current investigation has aimed at shedding light on the damage mechanism of turbine blades by studying a real case in a practical situation. Also, Concurrent with physical investigation, numerical simulation was performed to study the effect of particle impact into the blade.

2. Materials and Methods

A total of four samples from broken blades of stages 1 and 2 of a gas turbine were received for fracture investigations. The chemical composition of blades determined using the SEM-EDS technique is given in Table 1. The chemical compositions denote that the stage 1 sample, which bears higher temperatures of fuel ignition, contains higher concentrations of W, Cr and Co. The primary fractography investigations were carried out on the fractured surfaces of the blades using the scanning electron microscope (SEM). Then, few specimens from each blade sample were cut in a saw machine without applying any excessive heat, mounted, and polished with the appropriate sand papers and polishing nap. The prepared samples were etched in a reagent composed of 13 ml HCl, 8 ml HNO_3 and 5 gr Glycerol.

The microstructural constituents of the samples were examined by using an EDS detector attached to the SEM microscope. In order to study the effect of corrosion on the fractured surfaces of the blades the corrosion residuals and the intake gas to the turbine were analyzed using a gas chromatograph (GC) apparatus and X-ray fluorescence and diffraction techniques.

3. Results and Discussion

3.1. Fractography and microstructural characterization

Figs. 1a and 1b show the appearance of the damage occurred in the blades of stage 1 and 2. The visual inspections of the fractured surfaces in the samples showed only mechanical damages. Although the sample of stage 1 shows extensive cracking at the edge, the second sample has failed due to severe surface crack and splitting off the edge. Apparently, the blade of stage 2 may be subjected to high speed impacts which have caused cracking and breaking. It seems there were pieces of hard material separated from a defective first stage blade hit the others causing a chain of reactions to happen, resulting number of broken blades in the first and second stages.

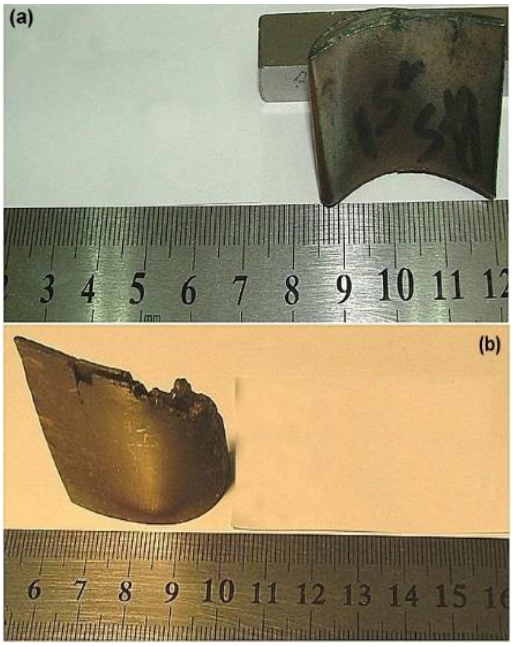

Fig. 1. Visual inspection of the damaged blades of (a) stage 1, and (b) stage 2 of a gas turbine.

Table 1. Chemical composition of the received blade samples of stage 1 and 2 (wt. %).

Element	Si	Mo	Re	W	Ta	Ni	Co	Cr	Ti	Al
Stage 1	--	0.54	1.18	8.32	1.81	63.49	9.27	8.17	0.71	6.54
Stage 2	1.52	--	--	7.61	4.62	72.45	1.78	3.19	1.02	7.92

Figs. 2a and 2b illustrate the existence of numerous cracks at the blades tips, which can be associated with thermomechanical fatigue. The magnified images of the blades tips exhibited in Fig. 3. shows that the cracking is accompanied by coating removals, some hot corrosion products. This, in turn, suggests that a combination of damaging factors including fatigue, corrosion and creep may counteract for the failure of the blades.

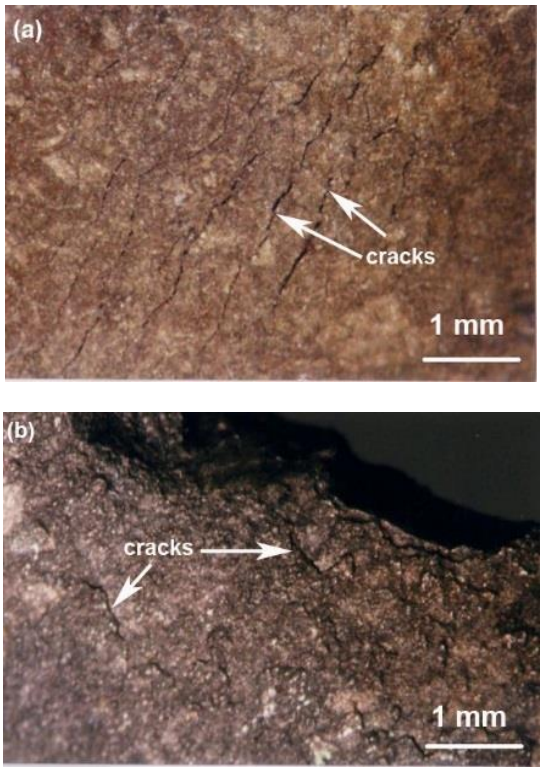

Fig. 2. Optical micrograph of the damaged blades, illustrating the existence of numerous cracks at the blades tips, (a) stage 1, and (b) stage 2 blades.

In summary, Figs. 2 and 3 imply that the damage in the second stage sample has been more severe than that in the first sample. This is well understood from more cracks and severe damage of the second sample blade tip. A closer look at the samples by SEM, shows in Fig. 4. , this Fig. shows that only on the second stage sample, traces of severely damaged thermal barrier coating layer on top of a diffusion layer were found. The same damage was not observed on the first stage sample. The damage of the TBC layer presumably due to mechanical hit of small particles separated from the first stage sample or carried by the fuel gas seems to be the starting point. Another issue which can harm the TBC layer is thermal expansion mismatches between the coating layers and the substrate, specifically when the blades are suffering excessive heats or frequent shut downs. By local damaging the TBC layer, the underneath layers are subjected to corrosion of oxidation and sulfidation as well as overheating. This, in turn, weakens the underneath layer and facilitate cracking due to thermomechanical fatigue. In case of the first stage sample, this scenario is postponed, because the synergy of corrosion and thermomechanical fatigue is not observed. However, the cracks are still originated from the inter-diffusion layer (under the TBC layer), where the greater thermal gradient present. However, in the case of the first stage sample, the TBC layer has effectively suppressed severe corrosion and only thermomechanical fatigue has caused cracking.

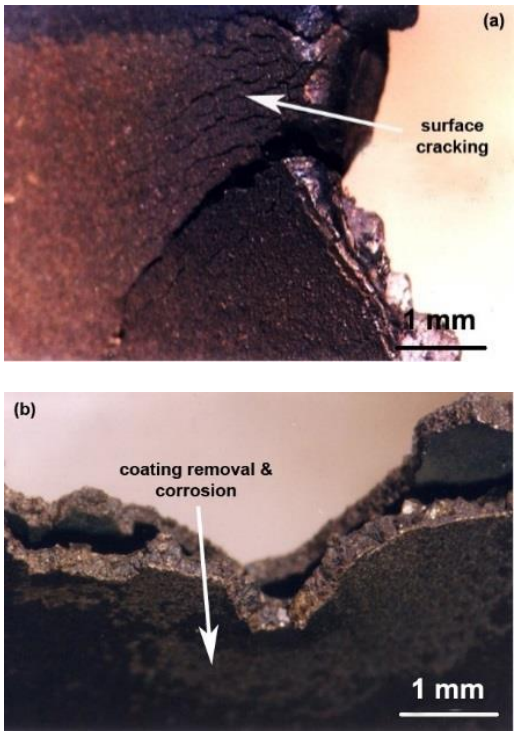

Fig. 3. Magnified view of the damaged blades: (a) stage 1, and (b) stage 2.

Fig. 5. shows the microstructure of the blades just below the TBC layer characterized by SEM. It is interesting that the observations are in agreement with the previous ones and imply that the sample of second stage (Fig. 5b), unlike to the first stage sample (Fig. 5a) has subjected to more excessive heat. This is elicited from the evolution of γ' precipitates (the cubic-formed precipitates) distributed in the γ matrix.

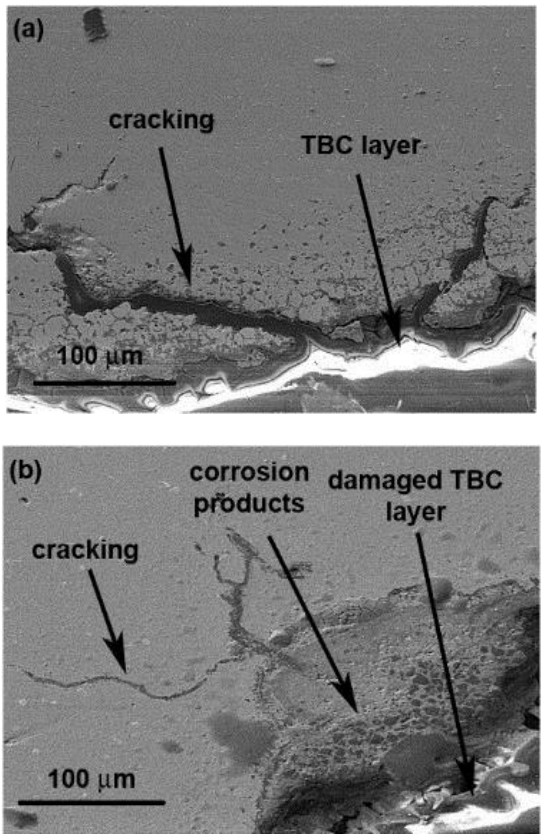

Fig. 4. SEM micrographs of the blade tips of (a) stage 1, and (b) stage 2, showing different cracking mechanisms and TBC layer conditions.

It is known that creep resistance is dependent on slowing the speed of dislocations within dual-phase structure of γ-γ′. Therefore, it is very important to have a uniform, well distributed fine γ′ phase in γ matrix for the superalloys. It has been well known that γ′ precipitates tend to coalesce and grow when subjected to heating for a long time. This phenomenon is clearly seen in the second stage sample and is attributed to the mechanical damage of the TBC layer, which has caused the overheating of the layers underneath. The coarsening of γ′ precipitates, which is termed as rafting, is a primary step of creep and substantially decreases the strength of the alloy. Therefore, in addition to corrosion and thermomechanical fatigue, creep should also be taken into account as a detrimental player in the scenario of cracking and damage of the second stage sample. Unlikely, Fig. 5a shows that the uniform distribution and size of the γ′ precipitates has remained unchanged in the first stage sample due to the fact that the TBC layer has played its role in making a barrier against excessive heating of the blade.

3.2. Chemical analysis results

3.2.1. Sampling from gas turbine secondary filtering system

As observed in the previous micrographs, corrosion plays an important role in the damage of the turbine blades and in particular the second stage ones. In order to understand the type of corrosion and its role in the process of observed failure, samples from the secondary filtering system of the gas turbine (dark powdery substance and dark liquid from the bottom of the cylinder) were collected and subjected to a centrifugal separating method used to evaluate different phases. The dark liquid sample was tested by GC apparatus and the results are given in Table 2. Besides, the hydrocarbons presented in the dark liquid were analyzed and quantified as presented in Table 3.

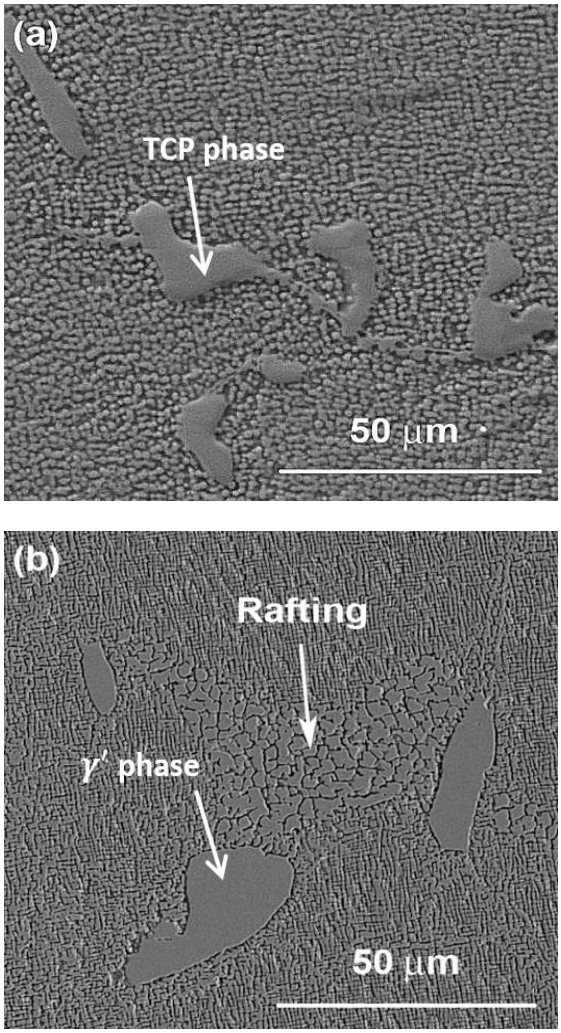

Fig. 5. Microstructure of (a) first stage sample, and (b) second stage sample, indicating the structure and distribution of γ′ precipitates distributed in the γ matrix.

Table 2. Chemical substances of dark liquid sample from the secondary filtering system.

Chemical Substance	Vol. %
Water	98
Sludge	1
Hydrocarbons	<1

Table 3. GC results of the hydrocarbons in the dark liquid sample.

Hydrocarbon Type	Weight %
nC13	0.12
nC14	<0.1
nC15	0.15
nC7	0.1
nC9, nC10, nC11, nC12	<0.1

Results showed that about 1 percent of the liquid sample collected from the bottom of secondary gas filtering cylinder was of heavy hydrocarbon branches, from C7 to C15. Therefore, lack of a suitable filtering system or a good filtering can increase the possibilities of injecting these into the gas chamber results in a sudden localized heat at nozzles and blade tips and causes them to excessive heat exposure. This deforms nozzles tips causing non-uniform distributions of flames in the chamber and partial heating of some first stage blades. At the same time, a fuel gas containing liquid hydrocarbons may burn inefficiently, produces excessive coke and sulfur which can attach the blades corrosively.

To evaluate the dark dust samples collected from the filter itself and its surrounding areas, the XRF and XRD techniques were employed. The results of XRF and XRD indicated that the dust is composed of Fe, S, Cl, Ca, Cr, Zr, Ni, Mo, Si and K, and the major substances were non-stoichiometric Fe_3S_4 and rusting powder Fe_2O_3. Having these chemical substances in the collected dust is confirming that the fuel gas contains considerable amounts of H_2S and moisture, resulting corrosion products along the fuel gas line, on the shell of the secondary filtering system and particularly on the turbine blades.

3.2.2. Sampling from the turbine exhaustion system

Some yellowish-green powdery particles were gathered from the turbine exhaustion system. The results of XRD and XRF analyses were performed on the samples and the results can be presented as in Table 4. The presence of manganese sulfate and iron/zinc sulfate are indicating that the fuel gas contains H_2S. After transforming H_2S to SO_2 during the burning process in the chamber, sulfuric acid forms in the presence of oxygen and moisture which is a corrosive agent. The acid reacts with iron, zinc, and others such as manganese to make sulfates as corrosion products.

Table 4. Analysis of samples collected from the turbine exhaustion system.

XRF Analysis, Elemental	Si, Fe, Ni, Cu, Zn, Mn, S, Cr, Ca, K
XRD Analysis, Chemical Substances	$MnSO_4$-$(7H_2O)$,$NiSi_4O_{10}(OH)_2$, $(Zn, Fe)SO_4$-$(6H_2O)$

3.2.3. Fuel gas analysis

Tables 5. and 6. givens the analyses of the fuel gas and the present mercaptans. The comparison of the fuel gas usually used in the turbine and that of recommended by the designer shows that the corrosive agents like H_2S and mercaptans are considerably higher than normal.

Table 5. Fuel gas analysis used in the gas turbine chamber.

Chemical compound	mol. %	
	Design condition	Average of the actual condition (within three years)
Methane (C1)	33.67	68.4
Ethane (C2)	8.64	40.3
Propane (C3)	6.556	7.1
ISO-Butane	3.39	0.86
N-Butane	1.10	1.75
ISO-Pentane	1.64	0.39
N-Pentane	1.995	0.41
Hexane	3.55	0.19
Heptanes	32.81	0.14
Nitrogen	1.17	1.7
Hydrogen Sulfide	1.625	1.73
Carbon Dioxide	4.16	4.15
Average Molecular Weight gr/mole	54.35	23.43
Gas Specific Gravity	1.88	0.54

Table 6. PPM of mercaptans in fuel gas for 2006.

Ethyl Mercaptan	44 PPM
Methyl Mercaptan	20 PPM
N-Propyl Mercaptan	5 PPM

The analysis of different fuel gas samples within three years revealed that the used gases were lighter and different from the typical fuel gas recommended by the design. It is known that the heat value for one mole of lighter gas is less than a heavier. For example, the heat value of the designed gas is 2360.3 kJ/mole and for the average gas used is calculated as about 997 kJ/mole. Therefore, lighter gases with lower heat values may have been harmful to the turbine by affecting its efficiency. Table 7. given the heat values produced per one mole of components gases. Chemical analysis results also showed that the fuel gas contains higher percentages of H_2S and mercaptans. This is an indication of having corrosion in the system. We noticed considerable amounts of manganese sulfate and iron/zinc sulfate as some yellowish-green substances gathered from the turbine exhaustion system. Samples gathered from the secondary filtering system and the turbine exhaustion affirm that the gas is becoming lighter, more sour, and with higher

PPM of mercaptans. A realistic expectation is higher corrosion and fouling, and possibly more surging with the compressors. Therefore, the corrosion and cracking of the second stage blades in not only due to the damage of TBC layer, but also the changes in the chemical composition of the used fuel gas.

Table 7. Heat values of the fuel gas components.

Fuel Gas Components	K J/mole of fuel gas	
	Design	Average within three years
Methane	270.033	548.5
Ethane	124.085	193.1
Propane	134.005	145.8
ISO-Butane	89.801	22.8
Butane	29.227	46.7
ISO-Pentane	50.266	12.7
N-Pentane	65.286	13.4
Hexane	136.624	7.5
Heptanes	1460.701	6.2
Total Heat	2360.33	996.9

4. Numerical Modeling

Particle flow code in two dimensions (PFC_2D) was used for investigation of the effect of particle impact into the blade [17].

4.1. Particle Flow Code3

In simulation of bonded particle model by PFC_2D, blade is represented as an assembly of circular disks bonded together at their contact points and confined by planar walls. The particles are bonded together at their contacts to simulate a competent material. There are two basic bonding models supported in PFC: a contact–bonded model and a parallel-bonded model. A contact bond approximates the mechanical behavior of high strength materials. The contact bond behaves as a parallel bond of radius zero. Thus, a contact bond does not have a radius or shear and normal stiffness's, as does a parallel bond, and cannot resist a bending moment; rather, it can only resist a force acting at the contact point. The contacts bonds are assigned with specified tensile and shear strength which allows resistance to tension and shear to exist at the contacts until the force at the contact exceeds the strength of the bond. The mechanics of PFC are described in detail in [5], and will not be repeater here. In order to generate a contact-bonded particle model for PFC_2D, using the routines provided in the following micro parameters should be define d: Ball-to-ball Contact Modulus, stiffness ratio KN over KS, ball friction coefficient, contact Norm al Bond Strength, contact Shear Bond Strength, Ratio of Standard Deviation to mean of bond strength both in normal and shear direct ion, and minimum Ball radius. Defining a parallel-bonded particle model requires three addition al micro parameters, which are: parallel-bond radius multiplier, parallel bond modulus, and parallel-bond stiffness ratio. In this study, bonded particle models are created by assuming that particles are joined and bonded together using the parallel-bonded model.

4.1.1. Preparing and Calibrating the Numerical Model

The standard process of generation of a PFC_2D assembly to represent a test model involves four steps: (a) particle generation and packing the particles, (b) isotropic stress installation, (c) floating particle elimination, and (d) bond installation.

(a) Particle generation and packing the particles (Fig. 6a): a rectangular vessel consisting of planar frictionless walls is created, and an assembly of particles is generated to fill the vessel. The wall normal stiffness is larger than the average particle normal stiffness to ensure that particle–wall overlap remains small. The particle diameters satisfy a uniform particle-size distribution bounded by Dmin and Dmax: to ensure reasonably tight initial packing, the number of particles is determined such that the overall porosity in the vessel is 8 %.The particles, at half their final size, are placed randomly such that no two particles overlap. The particle radii are then increased to their final values. (b) Install specified isotropic stress (Fig. 6b): the radii of all particles are reduced uniformly to achieve a specified isotropic stress, $\sigma 0$, defined as the average of the direct stresses. These stresses are measured by dividing the average of the total force acting on opposing walls by the area of the corresponding specimen cross-section. When constructing a blade material, $\sigma 0$ is set equal to approximately 1 MPa. This is done to reduce the magnitude of the locked-in forces that will develop after the parallel bonds are added.

c) Reduce the number of floating particles (Fig. 6c): an assembly of non-uniform sized circular cans contain a large number of floating particles that have 3 contacts. It is desirable to reduce the number of floating particles such that a denser bond network is obtained. By setting the number of ball contacts equal to 3 and the allowed number of floating particles to zero, we obtain a bonded assembly for which nearly all balls away from the specimen boundaries have at least three contacts.(d) Install parallel bonds (Fig. 6d): parallel bonds are installed throughout the assembly between all particles that are in near proximity. The grain property is also assigned. After the parallel bond installation, the direct tensile test was performed to calibrate the micro properties of particles and parallel bonds in the bonded particle model.

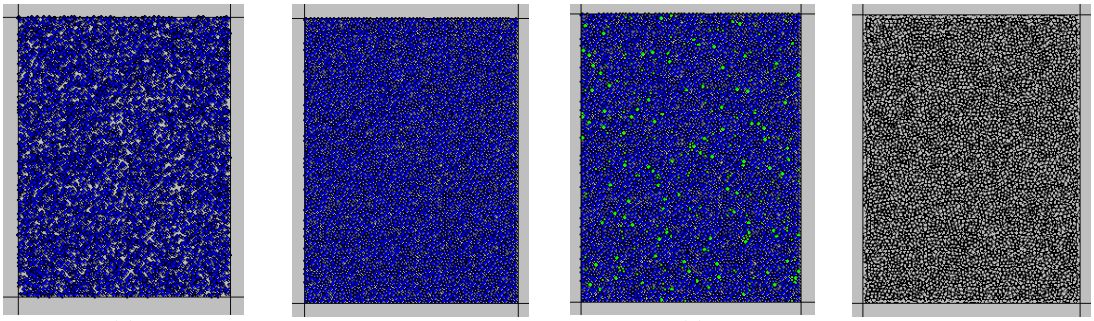

Fig. 6. The standard process of generation of a PFC$_2$D assembly to represent a test model involves four steps: (a) particle generation and packing the particles, (b) isotropic stress installation, (c) floating particle elimination, and (d) bond installation.

4.1.2. Direct Tensile Test

Direct tensile test was used to calibrate the tensile strength of specimen in PFC$_2$D model. Adopting the micro-properties listed in Table 8. and the standard calibration procedures [5,17] a calibrated PFC particle assembly was created. The geometry considered in the numerical tests was shown in Fig. 7b. The specimen was made of 5,615 particles. The disk was crushed by the upper and lower walls moved opposite from each other with a low speed of 0.016 m/s. Fig. 7a , b illustrate the failure patterns of the numerical and experimental tested samples, respectively. Tensile cracks were shown by yellow line. The failure planes experienced in numerical and laboratory tests are well matching. The numerical tensile strength and a comparison of its experimental measurements are denoted in Table 9. This table given a good accordance between numerical and experimental results.

Table 8. Micro properties used to represent the steel blade.

property	Value
Type of particle	Disc
Densiy (kg/m3)	3000
Minimum radius (mm)	0.27
Size ratio	1.56
Porosity ratio	0.05
Local damping coefficient	0.7
Contact young modulus (GPa)	12
Stiffness ratio (kn/ks)	1.7
Parallel bond radius muliplier	1.4
Youngs modulus of parallel bond (GPa)	1.7
Parallel bond stifness ratio (pb_kn/pb_ks)	3
Particle friction coefficien	0.5
Parallel normal strength, mean (MPa)	50
Parallel normal strength, std. dev (MPa)	5
Parallel shear strength, mean (MPa)	50
Parallel shear strength, std. dev (MPa)	5

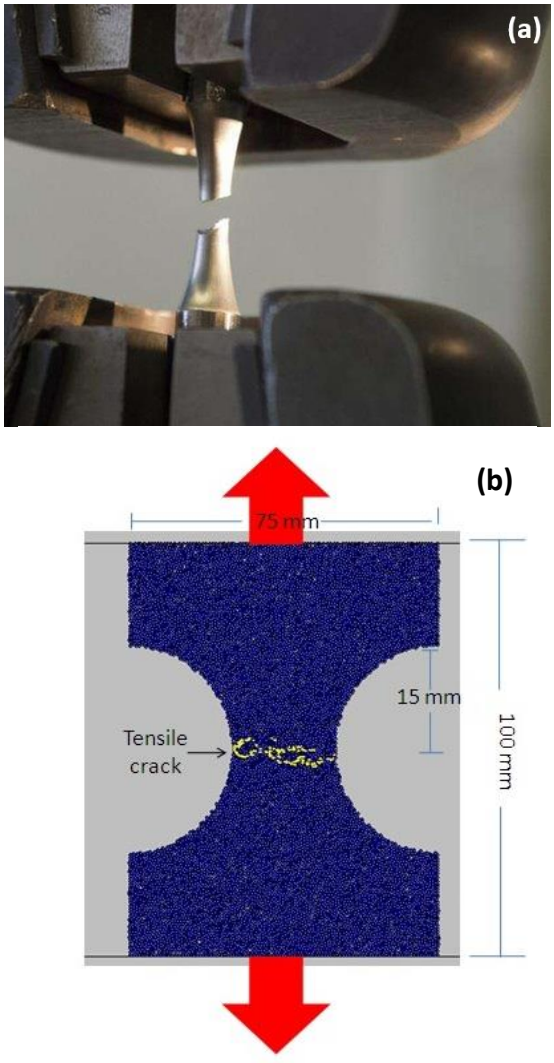

Fig. 7. Failure pattern in a) physical sample, b) PFC$_2$D model.

Table 9. Direct tensile strength of physical and numerical samples.

Physical tensile strength (MPa)	250
Numerical tensile strength (MPa)	259

4. 2. Numerical simulation of blade and particle

4.2.1. Preparing the Model

After calibration of PFC_2D, numerical simulation of blade and particle was simulated by creating a box model in the PFC_2D (Fig. 8a). The PFC specimen had the dimensions of 75×100 mm. A total of 11,179 disks with a minimum radius of 0.27 cm were used to make up initial model condition. After model generations, a particle was created in the right edge of the model (Fig. 8b). Round particle were considered to locate vertically at a distance of 5mm from the blade's internal wall (Fig. 8.). The particles diameters (b in Fig. 8.) for modeling were set at 1, 2, 4, and 6 mm, vertically located in front of the wall (a in Fig. 8.) at 0, 5, 10, and 30 mm from the blade tip. The particles hit the blades with the speed of 2 m/s and diffused into 0.2 mm in dept. In all simulations, blades were taken to be static and struck by the moving particle. Totally, twenty simulating performances for different modeling arrangements were executed to investigate the effects of particle diameter and its distance from the blade tip on any possible fracture patterns.

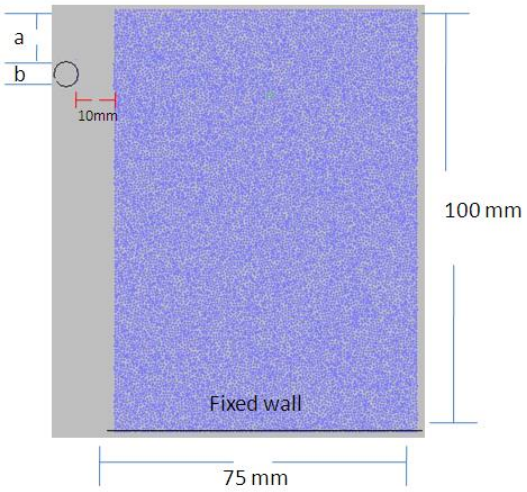

Fig. 8. Numerical simulation of blade and particle.

4.3. Fracture Patterns for Blades

Here, the effects of particle diameters and their spacing from the blades on their fracture patterns were discussed. The cracks colored by red and black are differentiating them as those initiated by shearing or tensile, respectively.

4.3.1. Vertical location of a particle from blade tip in 30mm distance

Fig. 9a, b, c and d shows the fracturing of blades as the results of them by particles with four different sizes.

Fig. 9. shows that the blade fracturing is caused by sliding between the disks and their splitting from each other. In all cases, cracks are initiated at particle-blade hitting interfaces and progressed in triangle forms through the remaining indentations. It can be said that by increasing the particle diameter, the sizes of indented areas remain approximately constant. As indentation depth was the same for all, only impact stress caused fracturing in all modeling. Then as the impact stresses are constant for all, the indentation areas remain unchanged too. If the indentation depth becomes larger, then it can be said that the intended areas are affected by disk dimension.

4.3.2. Vertical location of a particle from blade tip in 10mm distance

Fig. 10a, b, c and d shows the blades fracturing as the results of particles (1, 2, 4, and 6 mm in diameters) impacting to.

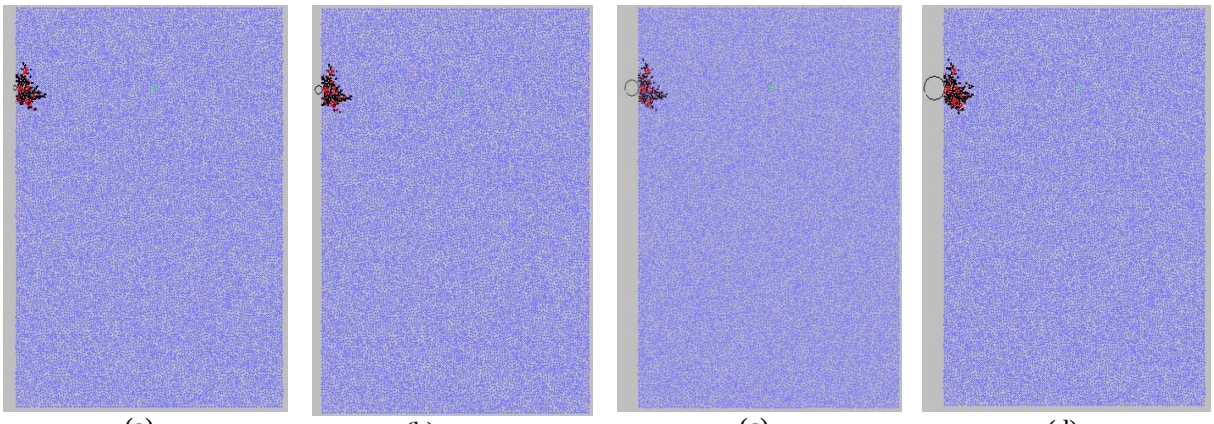

(a) (b) (c) (d)

Fig. 9. The fracturing of blades as a results of them by particles with four different diameter of, a) 1, b) 2, c) 4, and d) 6 mm.

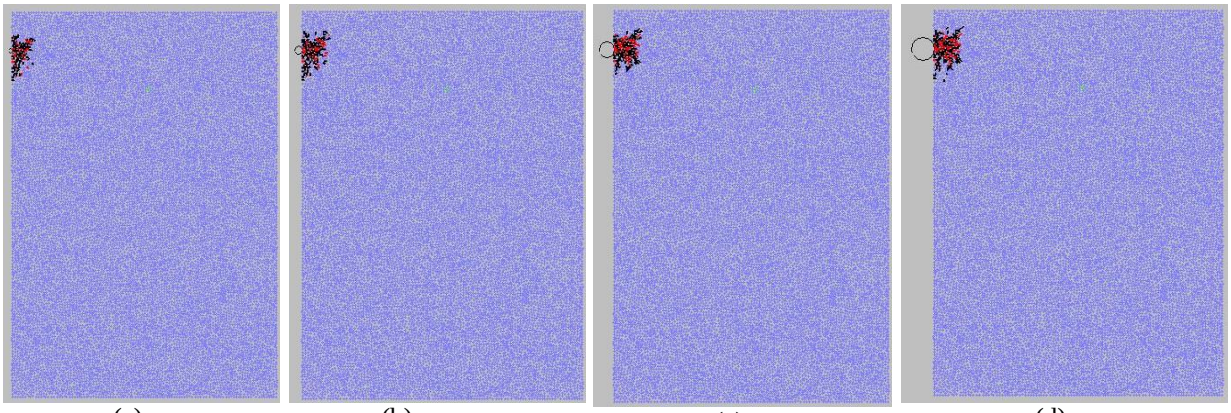

(a) (b) (c) (d)

Fig. 10. The fracturing of blades as a results of them by particles with four different diameter of, a)1, b) 2, c) 4, and d) 6 mm.

In all models, shear and tensile cracking initiate under the particles and propagate at indentation surfaces.

4.3.3. Vertical location of a particle from blade tip in 5mm distance

Fig. 11a, b, c and d shows the blades fracturing as the results of particles (1, 2, 4, and 6 mm in diameters) impacting to.
Tensile and shear cracking patterns on blades are showing crystals sliding and ruptures. These cracks initiate under the particles on blades surfaces and progress towards the tips and also the bulk. The results will be pieces of blades separated from their tips. The fracture patterns in all models are circular with constant fracture surface.

4.3.4. Vertical location of a particle from blade tip in 0mm distance

Fig. 12a, b, c and d shows the blades fracturing as the results of particles (1, 2, 4, and 6 mm in diameters) impacting to.

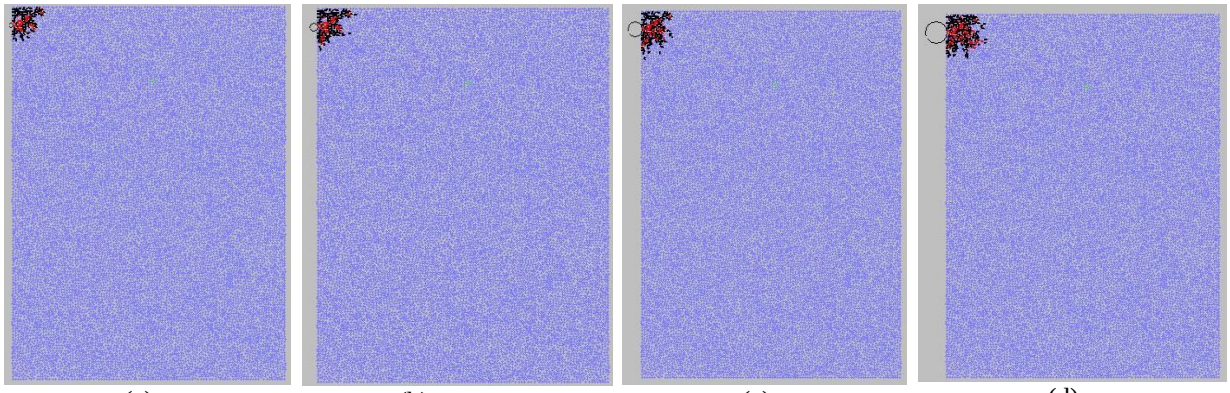

(a) (b) (c) (d)

Fig. 11. The fracturing of blades as a results of them by particles with four different diameter of, a) 1, b) 2, c) 4, and d) 6 mm.

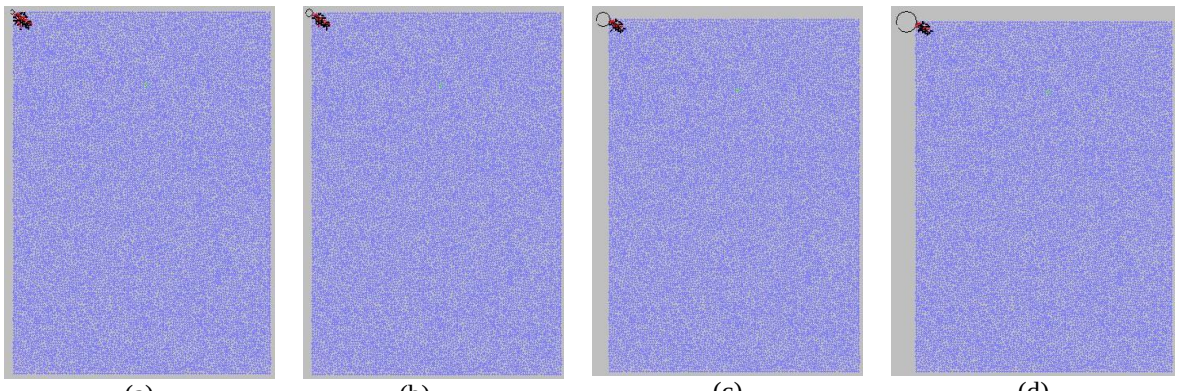

(a) (b) (c) (d)

Fig. 12. The fracturing of blades as a results of them by particles with four different diameter of, a) 1, b) 2, c) 4, and d) 6 mm.

In general, tensile and shear cracks initiate at the point of hitting blades by particles and they propagate under an angle of 45° through. The length and width of defected areas in all models are similar at 5mm and 2mm respectively. In this condition, only the blade tip will be flawed.
It can be said that when the distance between the particle and blade tip is constant then by increasing the particle diameter, the fracture pattern, the fracture surface, and the fracture mode stay unchanged.

5. Conclusions

1. All samples suffered excessive heat superficially. There were traces of oxidation/sulfidation products on the blades. However, for case of second stage blade the damage of the thermal barrier coating caused severe damage of the layers underneath by a combination of corrosion, thermomechanical fatigue and creep.
2. Thermal or mechanical shocks (Surging) and hitting by fine particles damage the thermal barrier coating layer and harm the blades. Although for case of the first stage blades cracking was postponed, the thermomechanical fatigue cracks still originated from the blade surface.
3. It was observed that the damage of the thermal barrier coating layer would lead to the overheating of the blades, promoting the rate of creep and coarsening of γ' precipitates, which is called rafting. This phenomenon was more sever in the second stage samples with more damaged protective layers.
4. It was found that the chemical composition of the fuel gas may increase the potential and rate of corrosion and damage to the blades. In this regard, the amounts of mercaptans and H_2S must get under control. Injecting lighter gas to the cylinder leads to higher temperatures which harm the blades and accelerate the deleterious processes such as hot corrosion and creep.
5. Numerical simulation shows that Different hitting points from the blade tip present various morphologies for the fracture pattern. When the distance is at 30mm, the fracture is triangular and the cracks run through the blade. At distance of 10, the fracture is also triangular with the cracks go towards the tip. At the distance of 5mm, the fracture is circular and there will be a particle separated from the blade tip. In the case of zero distance, a shear band with the length of 5mm and the width of 2mm under an angle of 45° propagate through the blade.

References

[1] S. S. Babu, S. A. David, J. M. Vitek, and M. K. Miller, Proc. of 43rd Int. Field Emission Symp., Moscow, (1996), 253.
[2] K. Chen, L. R. Zhao and J. S. Tse, Mater. Sci. Eng. A, 360(2003), 197.
[3] N. Warnken, D. Ma, M. Mathes and I. Steinbach, Mater. Sci. Eng. A, 413-414(2005), 267.
[4] T. Liang, H. Guo, H. Peng and S. Gong, J. Alloy. Compd, 509(2011), 8542
[5] D.O. Potyondy, P.A. Cundall, Int. J. Rock. Mech. Min. Sci., 41(2004), 1329.
[6] L. Wang, S. Wang, X. Song, Y. Liu, G. Xu, Int. J. Fatigue., 62(2014), 210.
[7] K. Wu, G. Liu, B. Hu, W. Ma, Y. Zhang, Y. Tao and J. Liu, Procedia Eng., 27(2012), 939.
[8] L. Zheng, G. Zhang, T. L. Lee, M. J. Gorley, Y. Wang, C. Xiao and Z. Li, Mater. Des., 61(2014), 61.
[9] P. Lukas, L. Kunz and M. Svoboda, Int. J. Fatigue., 27(2005), 1535.
[10] M. Nurbanasari, Abdurrachim, Case Stud. Eng. Fail. Anal., 2(2014), 54.
[11] V. Naga Bhushana Rao, I. N. Niranjan Kumar and K. Bala Prasad, Int. J. Eng. Sci. Technol., 6(2014), 43.
[12] G. N. Tret'yachenko, Strength Mater., (1971), 147.
[13] J. M. Gallardo, j. A. Rodriguez, and E. J. Herrera, Wear, 252(2002), 264.
[14] R. Viswanathan, Eng. Fail. Anali., 8(2001), 493.
[15] D. Dragomir-Stanciu, C. Oprişan, G. Ianuş and I. Vasile Crîşmaru, Procedia Technol., 12(2014), 329.
[16] T. Sadowski, P. Golewski, Comp. Mater. Sci., 50(2011), 1326.
[17] Itasca, PFC_2D Particle Flow Code in 2 Dimensions, Theory and background. Itasca Consulting Group, Minneapolis MN, Technical Report, (1999), 1–124.